

Characterisation of a large area silicon photomultiplier

A. Nagai^{1, *}, C. Alispach¹, V. Coco¹, D. della Volpe¹, M. Heller¹, T. Montaruli¹, S. Njoh¹ Y. Renier¹, I. Troyano-Pujadas¹,

1 Department de physique nucléaire et corpusculaire, Université de Genève, 24 Quai E. Ansermet, Switzerland

* Andrii.Nagai@unige.ch

Abstract

This paper illustrates the definition and the measurement methods of the main silicon photomultiplier (SiPM) features, such as photon detection efficiency as a function of over-voltage and wavelength, dark count rate, optical cross-talk, after-pulse probability. Moreover, several methods for the measurement of the breakdown voltage V_{BD} from the current-voltage IV curve, such as the “relative derivative”, the “inverse relative derivative”, the “second derivative”, the “third derivative” and the “IV model” are compared. These methods are applied to a very large area monolithic device: the hexagonal SiPM S10943-2832(X) device, of area (1 cm²), which has been developed in collaboration with Hamamatsu. We describe the measurements of the performance at room temperature of this device.

1 Introduction

In the last few years the interest in solid state photodetectors has grown significantly. In particular, SiPMs¹ have replaced traditional photomultiplier tubes (PMTs) in many applications. As a matter of fact, they are very compact, robust, lightweight, insensitive to magnetic fields and their operating parameters are highly stable across devices of the same type thanks to the high level of uniformity achieved by the solid state technology production technique. Also the absence of ageing caused by the integrated light over time, makes them particularly tailored for ground-based astrophysics [21]. These features allow them to operate even in the presence of high level of background light, thus increasing the duty cycle and then the physics reach. These advantages lead to the adoption of this technology in many applications and projects, not only operating in cryogenic environment, but also at room temperature.

Among these projects, the University of Geneva and a Consortium of Polish and Czech Institutions are proposing a single mirror small size telescope to CTA [12], called the SST-1M. The SST-1M camera employs the sensor described in this paper. To achieve the desired performance with the chosen optics, the camera of the SST-1M is composed by 1296 pixels, each of an angular opening of about 0.24°. This translates into a pixel linear size of about 2.32 cm. In order to have a spatial uniform response of the camera, the pixels should have a circular shape which ensures equal distance between pixel centres in every direction. The hexagon is the best possible shape to achieve this uniformity with minimum dead

space. Nonetheless, commercially available monolithic devices of comparable size have a square shape. The University of Geneva group developed a SiPM of hexagonal shape with the Hamamatsu company. A light funnel approaching the ideal Winston cone geometry was designed to be coupled to the SiPM and achieve the desired pixel size. The light-guide has hexagonal shape and has a compression factor of about a factor of 6 [11]. It is coated to maximise reflection of blue and UV light with almost perpendicular incidence onto the sensor.

This work reports on the characterisation studies done to validate the design and verify the performances of the SST-1M new sensor type. The main characteristics of the sensor are detailed in Tab. 1. The sensor area is around 93.6 mm² with a linear dimension of 10.4 mm flat-to-flat which ranks it among the world’s largest monolithic sensor.

¹Hamamatsu adopted the name Multi-Pixel Photon Counters or MPPCs

Nr. of channels	4
Cell size	$50 \times 50 \mu\text{m}^2$
Nr of cells (per channel)	9210
Fill Factor	61.5%
DCR (@ V_{op} per channel)	2.8-5.6 MHz
$C_{\mu cell}$ (@ V_{op} per channel)	85 fF
Cross-talk (@ V_{op} per channel)	10%
V_{BD} Temp. Coeff.	54 mV/C°
Gain (@ V_{op} per channel)	7.5×10^5

Table 1: S10943-2832(X) SiPM main characteristics provided by the producer at $T = 25$ °C. $V_{op} = V_{BD} + 2.8$ V.

2 The Hamamatsu S10943-2832(X) SiPM

The SiPM S10943-2832(X), shown in Fig. 1, has been designed in collaboration with Hamamatsu and is based on the so called LCT2 (Low Crosstalk) technology. Though Hamamatsu has further improved this technology (LCT5) we have adopted it for the camera of the SST-1M because at the moment of the sensor purchase the newer solution was not available. Currently, we evaluate that the slightly higher dark count rate (DCR) is not preventing the camera to have good performance if appropriately calibrated. Actually some dark count is useful for in-situ calibrations and further reduction of this rate increases the time needed to accumulate the statistics needed for precise calibrations.

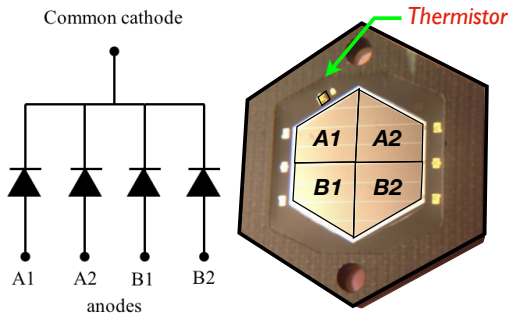


Figure 1: Picture of the Hamamatsu S10943-2832(X) SiPM (right) and its electric equivalent model (left).

²<http://ideasquare.web.cern.ch>

³ <http://www.tek.com/low-level-sensitive-and-specialty-instruments/series-6400-picoammeters-manual/model-6487-picoammeter>

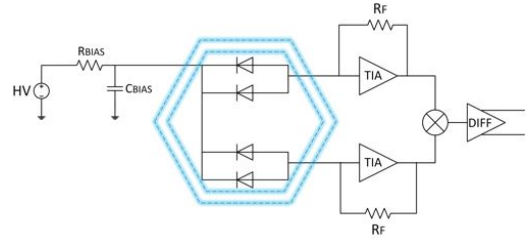


Figure 2: SiPM polarisation scheme and pre-amplifier topology used to sum up its four channels.

The sensor capacitance is directly related to its active area and this has an impact on the signal recharge time. Due to the large capacitance, signals have typical duration of about hundred ns, a too long time for the desired bandwidth of 250 MHz. This frequency is suitable for time durations of atmospheric showers induced by gamma-rays and cosmic rays. In order to reduce this time, signal shaping is needed by the front-end electronics. As shown in Fig. 1, the sensor has four independent anodes and a common cathode. This configuration allows to readout the 4 channels independently but there is a single bias for the whole sensor. In order to achieve a shorter signal, the four channels are summed up by using the topology shown in Fig. 2 that employs an active electronics based on operational amplifiers. To acquire the AC measurements presented in this article each SiPM channel was connected to an operational amplifier OPA846 and readout independently [2].

3 Static characterisation

All the laboratory measurements (i.e. static, dynamic and optical) are performed at room temperature $T = 25$ °C at the premises of IdeaSquare ² at CERN, where an experimental setup has been developed. The static characterisation (i.e. reverse and forward IV), is performed using a Keithley 6487 ³ pico-ammeter for bias supply and current measurements.

3.1 Forward IV characterisation

The forward IV characteristic curve of the SiPM is presented in Fig. 3. The IV curve shows a very small increase of the current when the polarisation voltage, V_{bias} , is below the threshold value, and a linear rapid current increase with V_{bias} above this threshold. A physical interpretation of this behaviour can be attempted starting from the ideal Shockley law [20], which expresses the forward current flowing through a $p-n$ diode as:

$$I = I_s \left[\exp \left(\frac{V_j}{\eta V_T} \right) - 1 \right], \quad (1)$$

where I_s is the reverse bias saturation current, V_j is the voltage across the junction, V_T is the thermal voltage and η is the ideality factor. The voltage V_j is the difference between the applied voltage V_{bias} and the voltage drop across the neutral region and the ohmic contacts on the two sides of the junction:

$$V_j = V_{bias} - IR_s \quad (2)$$

where usually $R_s \simeq 100 \Omega$.

Replacing V_j by V_{bias} in Eq. 1, we obtain:

$$V_{bias} = \eta V_T \left[\ln \left(\frac{I}{I_s} + 1 \right) \right] + IR_s. \quad (3)$$

The SiPM is composed by a given number of micro-cells (μcell), $N_{\mu\text{cell}}$. Each μcell can be represented by a diode connected in series with a quenching resistor R_q ⁴. Eq. 3 applies to each single μcell by adding an additional voltage drop on its quenching resistance R_q . Then for a full SiPM device with $N_{\mu\text{cell}}$ connected in parallel, Eq. 3 becomes:

$$V_{bias} = \eta V_T \left[\ln \left(\frac{I}{I_s} + 1 \right) \right] + I \frac{(R_s + R_q)}{N_{\mu\text{cell}}}. \quad (4)$$

The last term of Eq. 4 is negligible when I is small, while it dominates at high current ($I > 5 \text{ mA}$). In this regime, $R_s + R_q$ can be extracted from a linear fit of the forward IV characteristic curve in Fig. 3 ($I = a + bV_{bias}$, where a and b are free parameters of the fit):

$$R_q \Big|_{R_q \gg R_s} \simeq R_q + R_s = \frac{N_{\mu\text{cell}}}{b}. \quad (5)$$

⁴The μcell works in Geiger-Avalanche mode meaning that when a photon is absorbed, an electron-hole pair is created and the high electric field in the junction starts charge multiplication which produces an avalanche. If the field is not reduced the charge avalanche is stationary. By adding a resistor in parallel to the μcell , a voltage drop is produced by the current induced by the charge avalanche when flowing into the resistor. This drop reduces the field across the device thus quenching the avalanche. For this reason the SiPM are also referred to as an array of G-APDs - Geiger-Avalanche Photo-Diodes.

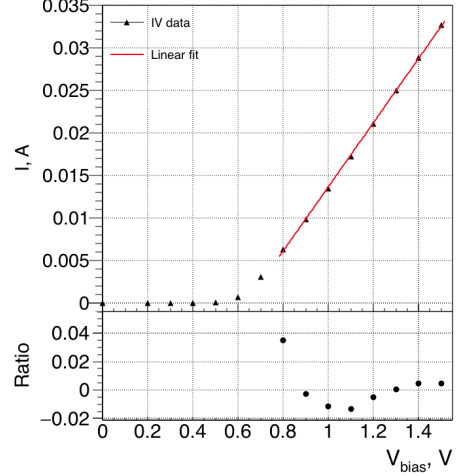


Figure 3: The forward IV characteristic curve of the Hamamatsu S10943-2832(X) SiPM. The linear fit (red line) and the $Ratio = (I_{data} - I_{fit}) \div I_{data}$ (bottom panel) are shown

3.2 Reverse IV characterisation

The reverse IV characteristic curve of the studied SiPM is presented in Fig. 4. Two main zones can be highlighted:

- the “pre-breakdown” region corresponding to V_{bias} below the breakdown voltage, V_{BD} , where the current increases slowly with V_{bias} . This dark current is due to the surface current (i.e. ionic impurities deposited on the surface during device fabrication) and the bulk current (i.e. thermal carriers generated in the depleted region (Shockley-Read-Hall (SRH) [23] [7]) and carriers resulting from trap-assisted or band-to-band tunnelling).
- the “post-breakdown” region, corresponding to V_{bias} above V_{BD} where the current increases much faster with V_{bias} . This trend is due to the Geiger avalanche triggered by the ionisation of free carriers within the depleted region (i.e. SRH thermal generation and tunnelling) and the associated effects (after-pulsing, prompt cross-talk and delayed cross-talk).

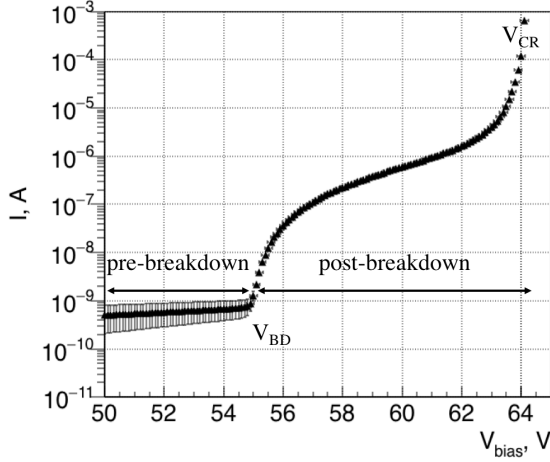


Figure 4: The reverse IV characteristic curve of the Hamamatsu S10943-2832(X) SiPM. Two different regions can be distinguished: *pre – breakdown* and *post – breakdown*.

The reverse IV measurements is commonly used for fast calculation of V_{BD} using different methods such as the “relative derivative” [4], the “inverse relative derivative” [6], the “second derivative” [13], the “third derivative” [16] and IV model methods [15], [1]. A brief review of each model as well as the comparison of results obtained with the different methods are presented below.

In the “relative derivative” and ‘inverse relative derivative’ methods it is assumed that the dark count rate and cross-talk probability are linearly depending on the bias voltage, so that the SiPM gain increases linearly with the over-voltage (difference between bias voltage and breakdown voltage). The measured current can be approximated as:

$$I = \alpha \times (V_{bias} - V_{BD})^n, \quad (6)$$

where I is the measured reverse current, α and n are the model constants which determine the shape of the reverse IV.

Therefore, the logarithmic derivative of Eq. 6 is:

$$\frac{d}{dV_{bias}} \ln(I) = \frac{n}{V_{bias} - V_{BD}}. \quad (7)$$

From Eq. 7 we can observe that the breakdown voltage can be calculated as a voltage at which $\frac{d}{dV_{bias}} \ln(I)$ has its maximum, as shown in Fig. 5. Hence it is possible to extract the breakdown voltage, called in the following V_{BD}^{1d} , by fitting the region around it with a spiky function such as a Landau, which nonetheless cannot reproduce the correct behaviour in the regions below and above the maximum. Therefore, the calculation of V_{BD} from “relative derivative” is limited.

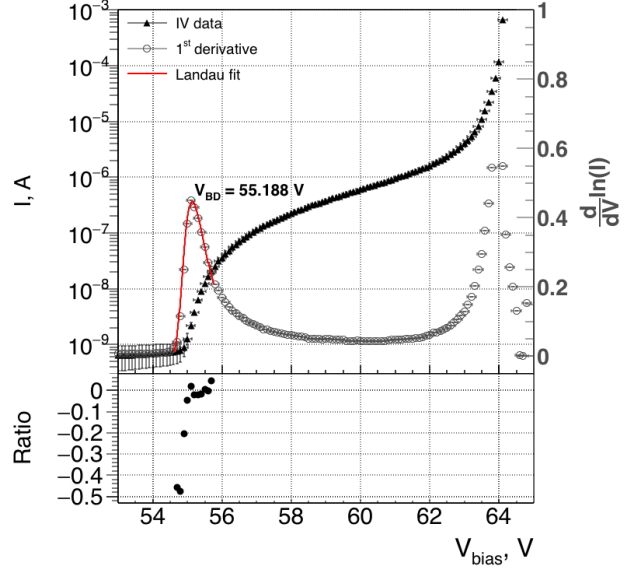


Figure 5: The reverse IV characteristic curve and its logarithmic derivative. A $V_{BD}^{1d} = 55.188$ V is extracted from the fit of the data with a Landau function shown with the red line. Also, the *Ratio* = $(\frac{d}{dV} \ln(I) - I_{fit}) \div \frac{d}{dV} \ln(I)$ is shown at the bottom of the figure.

Another option is the “inverse relative derivative”. From Eq. 6 we obtain:

$$1 / \frac{d}{dV} \ln(I) = \frac{V_{bias} - V_{BD}}{n}. \quad (8)$$

With this method (Fig. 6), the breakdown voltage $V_{BD}^{1dinv.}$ can be extracted as the voltage at which the “inverse relative derivative” is equal to zero, i.e. the intersection with the x-axis of the fitted line above V_{BD} .

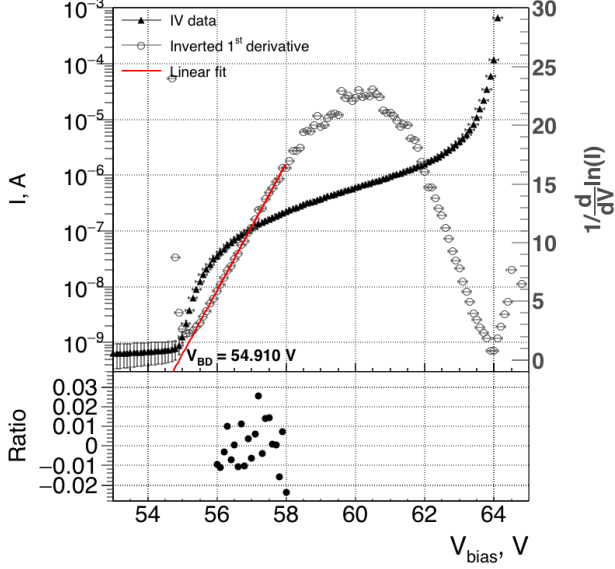


Figure 6: The reverse IV characteristic curve and its inverted logarithmic derivative. A value of $V_{BD}^{1dinv.} = 54.911$ V is determined as intercept of the x-axis of the right scale and the fitted inverted logarithmic derivative (red line). Also, the $Ratio = (1/\frac{d}{dV}\ln(I) - I_{fit}) \div 1/\frac{d}{dV}\ln(I)$ is shown at the bottom.

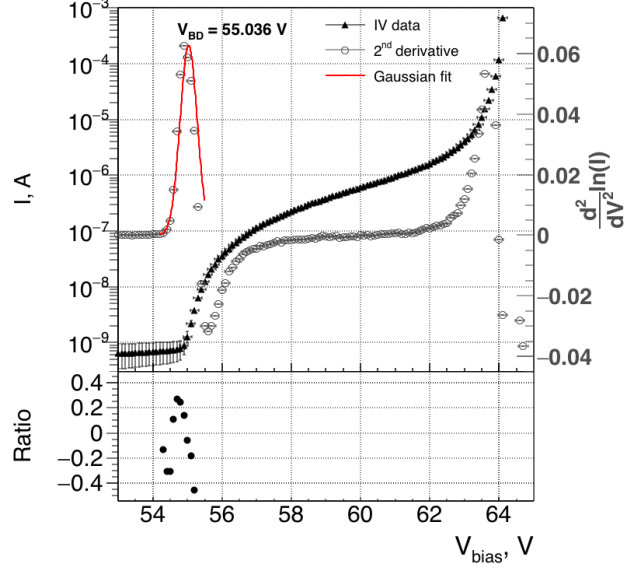


Figure 7: The reverse IV characteristic curve and its second logarithmic derivative curve. The $V_{BD}^{2d} = 54.96$ V is extracted from the fit of the peak. Also, the $Ratio = \left(\frac{d^2}{dV^2}\ln(I) - I_{fit} \right) \div \frac{d^2}{dV^2}\ln(I)$ is shown at the bottom of the figure.

In the “third derivative” method [16], authors have assumed that just above the breakdown voltage the presence of crosstalk (prompt and delayed) and after-pulses is negligible. Therefore, in this region the current is produced by charge avalanche in the μcell $q_{\mu\text{cell}}$ having an avalanche triggering probability P_{Geiger} . Assuming that both the avalanche charge and triggering probability are linear functions of V_{bias} , a quadratic relation for $V_{bias} \geq V_{BD}$ can be used:

$$I \sim q_{\mu\text{cell}}(V_{bias}) \cdot P_{Geiger}(V_{bias}) \sim (V_{bias} - V_{BD}) \cdot (V_{bias} - V_{BD}). \quad (9)$$

The “third derivative” method also assumes that the breakdown voltages in $q_{\mu\text{cell}}$ and P_{Geiger} are indeed two separate parameters: the “turn-on” $V_{turn-on}$ and “turn-off” $V_{turn-off}$ voltages [24]. $V_{turn-on}$ defines the regime in which the microcell initiates an avalanche and the current is related to the avalanche triggering probability P_{Geiger} . $V_{turn-off}$ is the voltage at which the voltage across the diode is reduced to quench the avalanche and the current is related to charge production $q_{\mu\text{cell}}$. Following the procedure found in Ref. [16], the third derivative of the reverse IV characteristic curve can be fitted with:

$$I = A \cdot \left[2 - \frac{h}{\sigma^2} (V_{bias} - V_{turn-on}) \right] \times \exp \left[-\frac{(V_{bias} - V_{turn-on})^2}{2\sigma^2} \right], \quad (10)$$

Also the “second derivative” method is commonly used (see [13], [17]) for the breakdown voltage determination. Here, the breakdown voltage V_{BD}^{2d} is calculated as the voltage corresponding to the maximum of the second derivative as shown in Fig. 7.

where $h = V_{turn-on} - V_{turn-off}$, A is the amplitude and σ is the standard deviation of the $V_{turn-on}$. The third derivative of the IV curve with the corresponding fit is presented in Fig. 8.

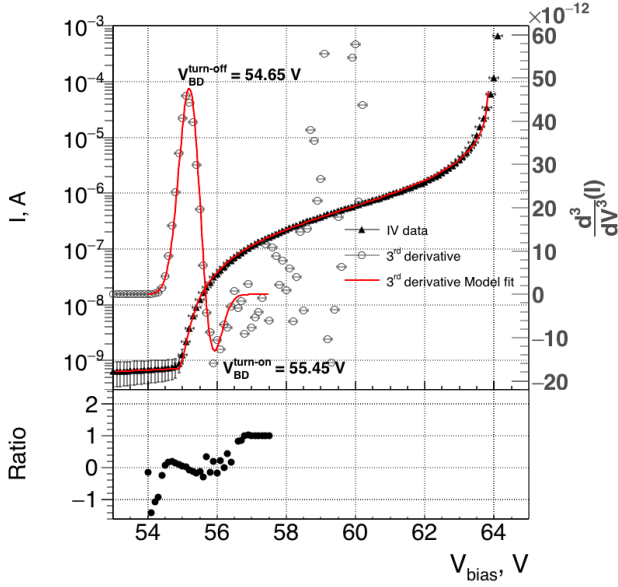


Figure 8: The reverse IV characteristic curve and its third derivative. The values of 54.65 V and 55.45 V is found for "turn-off" and "turn-on" V_{BD} from the fit of the curve. Also, the $Ratio = \left(\frac{d^3}{dV^3}(I) - I_{fit} \right) \div \frac{d^3}{dV^3}(I)$ is shown at the bottom of the figure.

A theoretical model of the reverse IV curve is proposed in Ref.s[15], [1]. In this model the IV curve contemplates several regimes depending on the bias voltage: (1) the "pre-breakdown" region below V_{BD} and (2) the "post-breakdown" region above V_{BD} , characterised itself by the "just-above", "transition", "far-above" and "post-second breakdown" zones (see Fig. 9):

- the "pre-breakdown" region, with relatively slow increase of the current related to the surface dark current, can be parametrised as:

$$I_{preBD}(V_{bias}) = e^{(a+b \cdot V_{bias})}, \quad (11)$$

where a and b - are free parameters;

- the "post-breakdown" region, with fast increase of the current, is the SiPM working region. In the "post-breakdown" region different regimes are distinguished:

- in the "just-above" region, the current is given by the number of free carriers $\frac{dN_{car}}{dt}$, the SiPM gain G_{SiPM} and the Geiger probability P_{Geiger} :

$$I_{postBD}(V_{bias}) = \frac{dN_{car}}{dt} \cdot G_{SiPM} \cdot P_{Geiger}, \quad (12)$$

where G_{SiPM} and P_{Geiger} can be expressed as:

$$G_{SiPM} = \frac{C_{\mu cell} \cdot (V_{bias} - V_{BD})}{e} = \frac{C_{\mu cell} \cdot \Delta V}{e}, \quad (13)$$

where $C_{\mu cell}$ is the SiPM microcell capacitance, $\Delta V = V_{bias} - V_{BD}$ is the over-voltage and:

$$P_{Geiger} = 1 - \exp(-PDE_{slope} \cdot \Delta V), \quad (14)$$

where PDE_{slope} is a parameter which depends on the type of SiPM (i.e. SiPM structure) and light wavelength. PDE_{slope} defines how fast P_{Geiger} increases with increasing ΔV for a given light wavelength. More details about PDE_{slope} will be given at Sec. 5.2 and 5.3;

- in the "far-above" region, the current is further amplified by correlated noise (i.e. after-pulsing and cross-talk effects). Due to their non-linear nature, the after-pulses are expected to be the dominant effect in this region leading to a multiplicative factor [19]:

$$G_{ap}(V_{bias}) = 1 + \frac{P_{ap}(V_{bias})}{1 - P_{ap}(V_{bias})}, \quad (15)$$

where $P_{ap}(V_{bias})$ is the probability that after-pulses will be produced. In this model, the after-pulse distribution in time is neglected for simplification. Therefore, the $P_{ap}(V_{bias})$ is proportional to the initial number of charges (i.e. SiPM Gain see Eq. 13) created in the avalanche. Thus, $P_{ap}(V_{bias})$ increases linearly with the over-voltage ΔV . The recursive nature of after-pulsing leads to a fast increase of the current until a "second breakdown region" is reached, at a critical voltage, V_{cr} , where $P_{ap}(V_{bias} = V_{cr}) = 1$:

$$P_{ap}(V_{bias}) = \frac{V_{bias} - V_{BD}}{V_{cr} - V_{BD}}; \quad (16)$$

- the "transition" region, that is located between the "just-above" and the "far-above" regions, where the current is a combination of the currents from these two regions;

- in the “post-second breakdown” region, runaway after-pulses and non-quenching effects lead to a very high current limited by the total series resistance of the device.

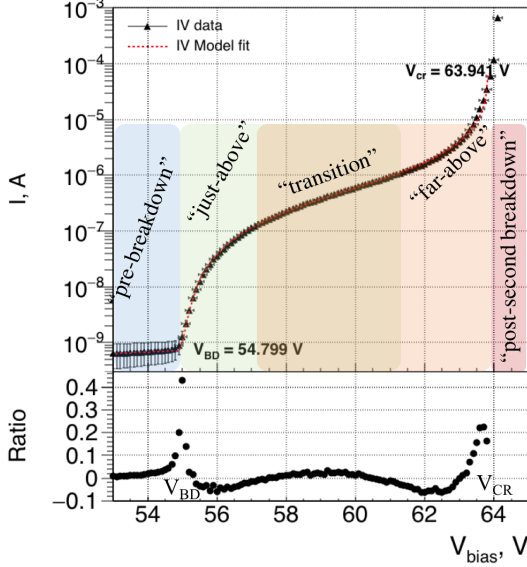


Figure 9: The reverse IV characteristic curve and its fit done with the IV model, from which a $V_{BD}^{IV-Model}$ of 54.621 V is extracted. The main regions (“pre-breakdown”, “just-above”, “transition”, “far-above” and “post-second breakdown”) are highlighted with different colours. Also, the $Ratio = \frac{I_{data} - I_{fit}}{I_{data}}$ is shown at the bottom of the figure.

All these phenomena are combined together into the fit function:

$$\begin{aligned}
 I(V_{bias}) &= \exp(a \cdot V_{bias} + b) + \frac{dN_{car}}{dt} \cdot P_{Geiger}(V_{bias}) \times \\
 &\times \left(1 + \frac{P_{ap}}{1 - P_{ap}} \right) \cdot C_{\mu cell} \cdot (V_{bias} - V_{BD}) = \\
 &= \exp(a \cdot V_{bias} + b) + \frac{dN_{car}}{dt} \cdot \frac{V_{cr} - V_{BD}}{V_{cr} - V_{bias}} \times \\
 &\times (1 - \exp[PDE_{slope} \cdot (V_{bias} - V_{BD})]) \times \\
 &\times C_{\mu cell} \cdot (V_{bias} - V_{BD}), \quad (17)
 \end{aligned}$$

where a , b , $\frac{dN_{car}}{dt}$, V_{cr} , V_{BD} , $C_{\mu cell}$, and PDE_{slope} are free parameters. This formula is used to fit the experimental IV characteristic curve shown in Fig. 9. The most significant difference between fit and data can be seen near V_{BD} and V_{cr} . The first one (near V_{BD}) is related to a fact, that SiPM biased below V_{BD} works like Avalanche Photodiode and this regime is not included in

IV Model. The difference near V_{cr} is related to a voltage drop on R_q .

The V_{BD} obtained with all the different DC methods varies from 54.65 V (“turn-off voltage from 3rd derivative model”) up to 55.45 V (“turn-on voltage from 3rd derivative model”), as shown in Tab. 2. The variation between obtained values is mostly related to the assumptions done to describe the IV curve. As an example, from Eq. 7, one can expect that $\frac{d}{dV_{bias}} \ln(I) \rightarrow \infty$. As shown in Fig. 5, this is not a case. Therefore, more complicated assumptions (like for the “IV Model”) should be used.

4 Dynamic characterisation

For the dynamic characterisation, the SiPM device is illuminated by low intensity LED pulses with different wavelengths (e.g. 405 nm, 420 nm, 470 nm, 505 nm, 530 nm and 572 nm). For each of the LED operating voltage, 10’000 waveforms are acquired by an oscilloscope, each 10 μs long (5’000 samples per waveform). The acquisition of waveforms is triggered with the same signal, produced by a pulse generator, which also triggered the LEDs. The readout window is chosen in order to have the trigger signal in the middle of the waveform. i.e. at 5 μs from the window start. Therefore, for a waveform we can distinguish two main intervals:

- “Dark interval” from 0 to 5 μs , when the device is operated in dark conditions. Only the SiPM thermal pulses enhanced by correlated noise, i.e. cross-talk (prompt and delayed) and after-pulses, are present (see Sec. 4.5 for more details);
- “LED” interval, from 5 to 10 μs , when the device is illuminated by LED light pulses but also thermal pulses are present. Both types of pulses are further affected by SiPM correlated noise (i.e. prompt and delayed cross-talk and after-pulses).

A typical waveform is shown in Fig. 10, where both Dark and LED intervals are marked and SiPM pulses from different sources are identified (thermal carriers⁵, LED light, after-pulses, optical prompt and delayed cross-talk).

“Dark intervals” are used to calculate the SiPM *Gain*, the V_{BD} , the dark count rate *DCR* and the optical cross-talk probability P_{XT} , while “LED intervals” are used to calculate the SiPM after-pulse probability and photon detection efficiency *PDE*.

The data acquisition system used for these measurements, consists of a pre-amp based on the transimpedance amplifier OPA846, an oscilloscope Lecroy 620Zi for the waveform acquisition (a bandwidth of 20MHz is used to reduce the influence of the electronic

⁵also known as dark count rate or *DCR*

	AC	DC					IV Model	
	Gain vs. V_{bias}	derivative				turn-on		turn-off
		1 st	1 st inverse	2 nd	3 rd			
$V_{BD}(V)$	54.699	55.188	54.911	54.960	55.45	54.65	54.799	
$\sigma_{stat.}(mV)$	± 17	± 46	± 100	± 30	50	50	± 1	
$\sigma_{sys.}(mV)$		± 25						
$V_{BD}^{AC} - V_{BD}, (mV)$		-489	-212	-261	-751	49	-100	

Table 2: The breakdown voltage obtained from the $Gain$ vs. V_{bias} dynamic (AC) measurement is presented as well as results from static (DC) measurements of the reverse IV curve methods with statistics ($\sigma_{stat.}$) and systematic ($\sigma_{sys.}$) errors for the Hamamatsu S10943-2832(X) SiPM. The difference between AC and each DC measurements is also provided.

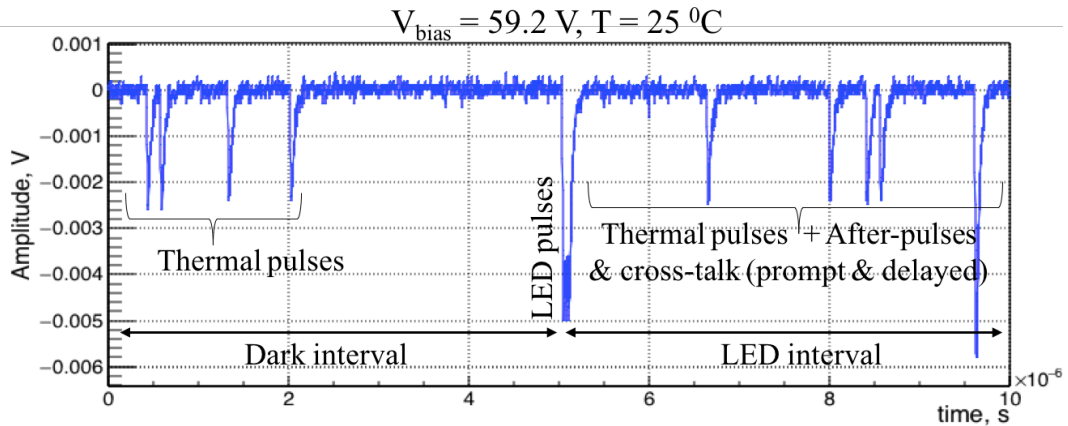


Figure 10: Typical waveform of a SiPM with signals coming from different sources: thermal carriers, light from LED, after-pulses and optical cross-talk (prompt and delayed).

noise) and a voltmeter Keithley 6487 as SiPM bias supply. For each LEDs of different wavelengths, the over-voltage ΔV is varied in the range $1 \text{ V} < \Delta V < 8 \text{ V}$, to cover the full working range of device (see Sec. 3.2).

4.1 Automatic data analysis procedure

The experimental data acquired in dynamic mode are analysed with an automatic procedure for data analysis, developed in the ROOT data Analysis Framework⁶. The waveforms acquired with the oscilloscope are used to create root-ntuples storing SiPM pulse templates. The steps of the analysis are the following:

- the construction of a template of a typical SiPM pulse shape at given working condition;
- a pulse finding procedure to identify SiPM pulses (i.e. a single pulse⁷ or a train of pulses⁸) and their relative time spacing;
- a template subtraction to reconstruct only the SiPM pulses in a train of pulses;
- a pulse shape determination to calculate the main features of the SiPM pulses as showed in Ref. 11.

The SiPM pulse characteristics, such as the baseline, time position and amplitude, rise time and decay time, charge Q , t_{before} ⁹ and t_{after} ¹⁰, are determined for different values of V_{bias} and of the temperature T . More details on the developed analysis procedure can be found in the Ref.[18].

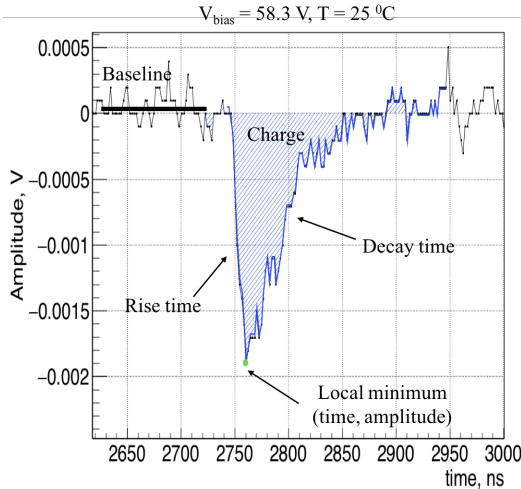


Figure 11: Typical SiPM pulse for a single photon equivalent (1 p.e.) on top of which its main characteristics are indicated.

⁶<https://root.cern.ch>

⁷A SiPM signal separated by the neighbouring pulses by a time interval longer than its recovery time.

⁸Two or more signals within a time interval shorter than the SiPM recovery time.

⁹Time difference between the analysed pulse and the previous one.

¹⁰Time difference between the analysed pulse and the following one.

4.2 SiPM Gain

The SiPM gain G is defined as the number of charges created in one avalanche in one μcell and it can be expressed as:

$$\begin{aligned} \text{Gain} &= \frac{Q}{e} = \frac{C_{\mu\text{cell}} \cdot (V_{\text{bias}} - V_{BD})}{e} = \\ &= \frac{C_{\mu\text{cell}} \cdot \Delta V}{e}, \end{aligned} \quad (18)$$

where Q is the avalanche charge, $C_{\mu\text{cell}}$ is the μcell capacitance and V_{BD} is the breakdown voltage.

Experimentally, the SiPM gain can be calculated from the time integration of the device signals:

$$\text{Gain} = \frac{Q}{e} = \frac{1}{G_{\text{Amp}} \cdot e} \cdot \frac{1}{R} \int V(t) dt, \quad (19)$$

where G_{Amp} is the amplifier gain, R is the amplifier input impedance ($R = 50\Omega$), $V(t)$ is the pulse amplitude and $\int V(t) dt$ is the area under the SiPM signal.

As can be seen in Fig. 12, the gain increases linearly with V_{bias} as expected from Eq. 18.

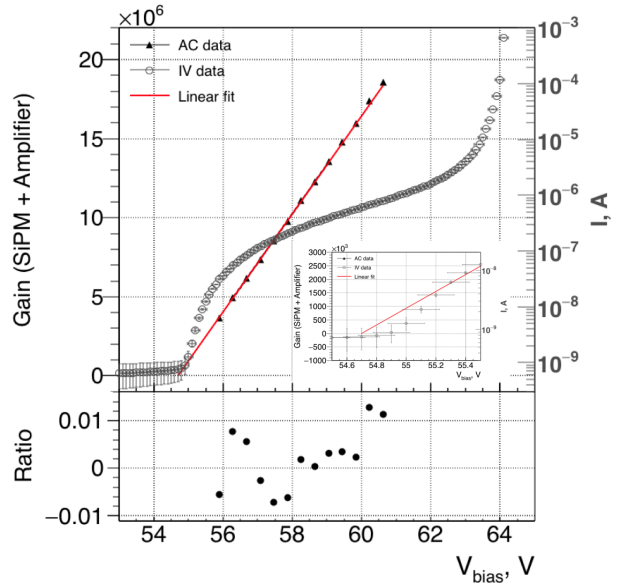


Figure 12: Gain of the amplified signal vs. V_{bias} for the Hamamatsu S10943-2832(X). The V_{BD} of 54.699 V is found at the intersection of the linear fit with the x-axis. The reverse IV curve with a zoom near V_{BD} are shown and the difference between the linear fit and the IV data can be seen in a broad V_{bias} range. Also, the ratio, defined as the difference between the experimental data and the fit function values divided by the experimental data is shown.

4.3 Breakdown Voltage, V_{BD}

The breakdown voltage of a SiPM device represents the voltage above which the electrical field inside the depleted region of a μ cell is high enough that any free carrier (created by an absorbed photon or by a thermally generated carrier) can trigger an avalanche. Experimentally, the breakdown voltage from AC measurements, V_{BD}^{AC} , can be determined from the curve of the gain as a function of V_{bias} (Fig. 12) by extrapolating the linear fit to zero. The measured value is $V_{BD}^{AC} = 54.699 \pm 0.017$ V. The comparison between this value and those obtained from reverse IV curve static (DC) methods (see Sec. 3.2) are presented in Tab. 2. We can observe significant differences between the dynamic measurement of the breakdown voltage and the static ones. The value of the V_{BD}^{AC} is a few hundreds of mV smaller than V_{BD} from the IV methods (except for the case of $V_{BD}^{turn-off}$ voltage from the 3rd derivative method). This discrepancy reflects the fundamental difference in the physics of the “breakdown” voltage obtained with these methods [15] [16] [24]. The IV static measurement is sensitive to the onset of the avalanche phenomenon and it determines the breakdown voltage as defined by the fundamental papers of McIntyre (named as “turn-on” voltage) [14]. The AC/gain linearity method determines the voltage across the diode when the avalanche is quenched (named as “turn-off” voltage). The latter is naturally lower than the former and our results are consistent with this expectation. This also explains why we find the smallest discrepancy between V_{BD}^{AC} and the result of the 3rd derivative method.

4.4 SiPM micro-cell capacitance $C_{\mu cell}$

The SiPM micro-cell capacitance $C_{\mu cell}$ can be calculated from Eq. 18 and Eq. 19, as:

$$C_{\mu cell} = \frac{Gain \cdot e}{\Delta V} = \frac{q}{\Delta V \cdot e} \cdot \frac{1}{G_{Amp}} \cdot \frac{1}{R} \int V(t) dt. \quad (20)$$

Since, the amplifier gain G_{Amp} changes with frequency, for future calculations we assume $C_{\mu cell}$ of 85 fF, as provided by Hamamatsu (See Tab. 1). The $C_{\mu cell}$ is related to micro-cell geometry, through the parallel plane capacitance equation:

$$C_{\mu cell} = \epsilon_0 \cdot \epsilon_{Si} \times \frac{A}{d} \quad (21)$$

where $\epsilon_0 = 8.854 \times 10^{-14}$ F/cm is the permittivity of free space, $\epsilon_{Si} = 11.9$ is the silicon dielectric constant, $A = 50 \times 50 \times 0.615 \mu m^2$ is the active area reduced by the geometrical fill factor of 0.615 and d is the depletion thickness of the micro-cell. Therefore, from this formula, the resulting depletion thickness is $d = 1.9 \mu m$.

4.5 The SiPM noise

The SiPM noise is a limiting factor for low-light level applications of SiPMs (from one to few photons). The

various mechanisms contributing to the SiPM noise can be classified in two main categories: the primary, or uncorrelated noise, which is independent from light conditions and is also referred to as dark count rate, DCR ; the secondary or correlated noise.

The DCR represents the number of output pulses per second produced when the device is in the dark by the following physical phenomena conditions. The dominating effect at room temperatures is the thermal generated carriers. When a SiPM is operated at high ΔV and the electric field across the junction increases, the electrons can tunnel through the band-gap via trap levels. In this case, the thermal generated carriers are amplified by trap-assisted tunnelling mechanism. In addition, the generation rate can be enhanced by the Poole-Frankel effect [10], also known as band-to-band tunnelling. The electric field increase augments the tunnelling of electrons directly from the valence band into the conduction band. Therefore, at a given temperature, the DCR is determined by the number of free carriers N_{car} enhanced by electrical field effects (i.e. trap-assisted and band-to-band tunnelings) at high ΔV and the probability that carriers trigger an avalanche (i.e. Geiger probability P_{Geiger}). Consequently, a simple empirical formula for the DCR can be approximated as:

$$DCR = N_{car} \cdot exp(b \cdot \Delta V) \cdot P_{Geiger}, \quad (22)$$

where b is a free parameter describing the increase of DCR with over-voltage due to electrical field effects.

Secondary, or correlated, noise is made by optical cross-talk and after-pulsing, induced by a primary avalanche previously generated by a noise source or by detected light photons. During the primary avalanche multiplication process, external photons are emitted due to hot carrier luminescence phenomena [9]. These photons may cause to:

- Prompt optical cross-talk, when external photons start secondary avalanches in one or more neighbour μ cells. Therefore, the prompt cross-talk probability P_{XT} can be expressed as:

$$P_{XT} = Gain \cdot P_{hv} \cdot P_{Geiger}, \quad (23)$$

where P_{hv} is the probability that external photons will be emitted, $Gain$ is the SiPM gain, which is the number of charges created during primary avalanche multiplication (see Eq. 18).

- Delayed optical cross-talk, when external photons absorbed in non-depleted regions of the device (i.s. substrate) and produce the carrier that can drift through depleted region and trigger secondary avalanche. Carrier diffusion time determines the delay time.

After-pulsing occurs when, during the primary avalanche multiplication process, one or more carriers are captured by trap levels in the micro-cell junction depletion layer and released after some time, triggering a secondary avalanche discharge correlated to the primary one. Therefore, the after-pulse probability P_{ap} can be approximated as:

$$P_{ap} = Gain \cdot P_{trap} \cdot P_{Geiger}, \quad (24)$$

where P_{trap} is the probability that a carrier will be trapped.

4.5.1 Dark count rate, DCR

As it is mentioned at the beginning of Sec. 4, in a window of about $5 \mu s$ preceding the LED trigger, the device is considered as operated in dark conditions. This time interval is used to calculate the dark count rate DCR .

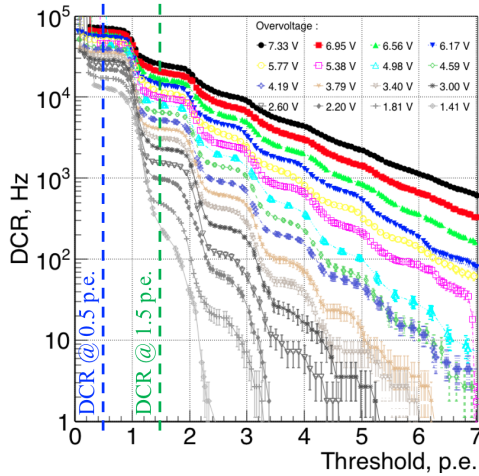


Figure 13: DCR vs. threshold for different values of ΔV for the Hamamatsu S10943-2832(X) SiPM. The blue and green vertical lines represent the DCR at 0.5 p.e. and 1.5 p.e. thresholds, respectively.

The DCR as a function of a discriminating threshold (in p.e.) at a given ΔV is calculated by counting the number of SiPM pulses with amplitude above the threshold (see Fig. 13). The DCR at the thresholds of 0.5 and 1.5 p.e. as a function of the over-voltage is presented in Fig. 14.

The measured DCR at the 0.5 p.e. threshold is fit using Eq. 22. A PDE_{slope}^{DCR} of 0.372 is found, of which the physical interpretation is given in Sec. 5.3. The measured DCR at 1.5 p.e. and higher thresholds includes optical cross talk and pile-up effects. Therefore it is approximated by a convolution of Eq. 22 and Eq. 23:

$$DCR_{1.5 \text{ p.e.}} = N_{car} \cdot exp(b \cdot \Delta V) \times P_{Geiger}^{DCR} \cdot Gain \cdot P_{hv} \cdot P_{Geiger}^{P_{XT}} \quad (25)$$

where P_{Geiger}^{DCR} is the probability that a free carrier initiates an avalanche, and $P_{Geiger}^{P_{XT}}$ is the probability that an external photon (emitted by hot carrier luminescence) will be absorbed and initiate an avalanche too. In general, free carriers and luminescence photons are absorbed at different depths of SiPM active areas. Therefore, $P_{Geiger}^{DCR} \neq P_{Geiger}^{P_{XT}}$. We can observe good agreement between experimental data and fit curves in both cases (DCR at 0.5 and 1.5 p.e. thresholds).

The DCR at 0.5 p.e. threshold vary from 10 kHz/mm^2 at $\Delta V = 1.5 \text{ V}$ up to 60 kHz/mm^2 at $\Delta V = 7 \text{ V}$.

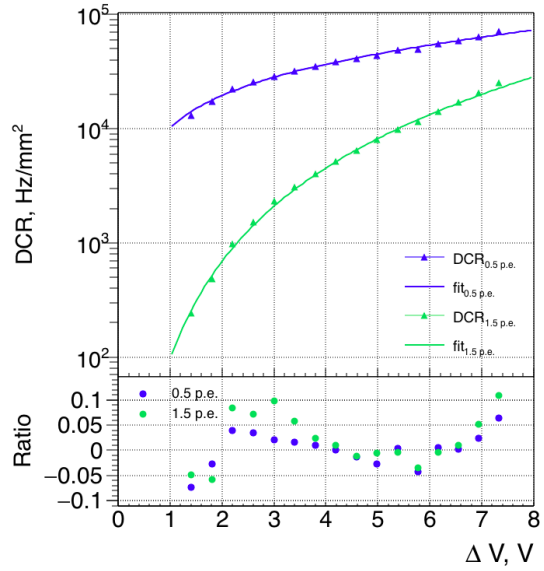


Figure 14: DCR vs. ΔV for the Hamamatsu S10943-2832(X) SiPM. The results are presented for the 0.5 p.e. (blue) and the 1.5 p.e. threshold (green). Also, the $Ratio = (DCR_{data} - DCR_{fit}) \div DCR_{data}$ for the 0.5 (blue) and 1.5 (green) p.e. thresholds are shown.

4.5.2 Prompt cross-talk probability, P_{XT}

Developed automatic data analysis can identify pulses inside a train if they are separated by more than 10 ns in time. Therefore, we can assume that the DCR at 1.5 p.e. threshold is caused only by the cross-talk probability, P_{XT} , it can be calculated as:

$$P_{XT} = \frac{DCR_{1.5p.e.}}{DCR_{0.5p.e.}}. \quad (26)$$

The DCR at 1.5 p.e. threshold is enhanced by the pile up effect. The total number of pile up pulses within

a given time interval τ can be calculated as:

$$\begin{aligned} N_{total} &= N_{2p} + N_{3p} + N_{4p} + \dots = \\ &= 2 \cdot \tau \cdot DCR_{0.5p.e.}^2 + 2 \cdot \tau^2 \cdot DCR_{0.5p.e.}^3 + 2 \cdot \tau^3 \cdot DCR_{0.5p.e.}^4 + \dots = \\ &= \frac{2 \cdot \tau \cdot DCR_{0.5p.e.}^2}{1 - \tau \cdot DCR_{0.5p.e.}}, \quad (27) \end{aligned}$$

where N_{2p}, N_{3p}, N_{4p} are the numbers of 2, 3 and 4 overlapping SiPM pulses during the given time interval τ . For our analysis $\tau = 10 \text{ ns}$.

The P_{XT} corrected for the pile up effect can be calculated as:

$$P_{XT}^{Corrected} = \frac{DCR_{1.5p.e.} - N_{total}}{DCR_{0.5p.e.} + N_{total}}. \quad (28)$$

In Fig. 15 the optical cross-talk probability, P_{XT} , as a function of the over-voltage, ΔV , is shown (blue dots) together with the corrected one (green dots).

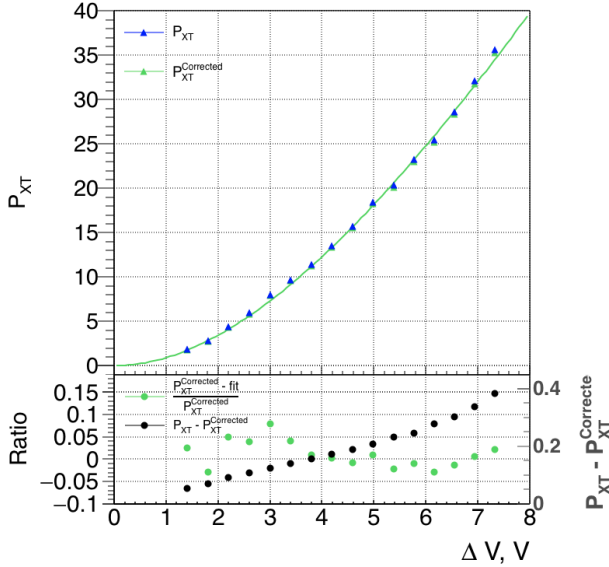


Figure 15: P_{XT} vs ΔV of the Hamamatsu S10943-2832(X) SiPM with ($P_{XT}^{Corrected}$) and without (P_{XT}) correction for the pile up effect. Also the difference between $P_{XT}^{Corrected}$ and P_{XT} is shown in the bottom plot, as well as $Ratio = \left(P_{XT}^{Corrected} - P_{XT}^{fit} \right) \div P_{XT}^{Corrected}$.

The $P_{XT}^{Corrected}$ is approximated by Eq. 23 and good agreement is found between the data and the proposed fit function. Taking into account $C_{\mu cell}$ of 85 fF (See Tab. 1), two free parameters $P_{h\nu}$ and $PDE_{slope}^{P_{XT}}$ are found from the fit. We find that on average $P_{h\nu} = 1.51 \times 10^{-5}$ photons with sufficient energy can be emitted by one carrier crossing the junction during avalanche multiplication. This value is in reasonable agreement with Lacaita [3], who found 2.9×10^{-5} for photons with energy higher

than 1.14 eV (or $\lambda = 1000 \text{ nm}$). The physical interpretation for found $PDE_{slope}^{P_{XT}}$ of 0.12 will be given in Section 5.3.

4.5.3 After-pulse and delayed cross-talk probabilities, $P_{delayed}$

As it is already mentioned in Sec. 4 the ‘‘Dark interval’’ contains the thermally generated pulses (i.e. DCR) enhanced by optical cross-talk (prompt and delayed) and after-pulses. Therefore, the ‘‘Dark interval’’ is used to calculate the after-pulses and delayed cross-talk probabilities $P_{delayed}$ as:

$$\begin{aligned} \langle N_{delayed} \rangle &= \langle N_{av}^{prim} \rangle \times \\ &\times (P_{delayed} + P_{delayed}^2 + P_{delayed}^3 + \dots) = \\ &= \langle N_{av}^{prim} \rangle \frac{P_{delayed}}{1 - P_{delayed}} \Rightarrow \\ \Rightarrow P_{delayed} &= \frac{\langle N_{delayed} \rangle}{\langle N_{av}^{prim} \rangle + \langle N_{delayed} \rangle}, \quad (29) \end{aligned}$$

where $\langle N_{delayed} \rangle$ and $\langle N_{av}^{prim} \rangle$ are the average numbers of detected after-pulses plus delayed cross-talk and primary avalanches during the ‘‘Dark interval’’, respectively.

Eq. 29 already contains the probability that every after-pulse can produce itself another avalanche, of which carriers may be trapped too and lead to a production of after-pulsing cascades. Therefore, the $\langle N_{av}^{prim} \rangle$ is determined only by thermally generated carriers and correlated prompt cross-talk $P_{XT}^{Corrected}$:

$$\langle N_{av}^{prim} \rangle = \langle N_t \rangle \times \left(1 + \frac{P_{XT}^{Corrected}}{100\%} \right). \quad (30)$$

The $P_{XT}^{Corrected}$ is already calculated in Sec. 4.5.2 and $\langle N_t \rangle$ is calculated in the following. The distribution of the local minima over the ‘‘Dark interval’’ is presented in Fig. 16. Each of the observed peaks is related to a certain number of photoelectrons p.e., which is expected to be Poisson distributed. However, the presented distribution is distorted due to correlated noise (i.e. after-pulses, prompt and delayed cross-talk). Nevertheless, the ‘‘0 p.e.’’ peak is not affected by after-pulses and optical cross-talk (prompt and delayed cross-talk) and can be used to determine the average number of thermally generated carriers $\langle N_t \rangle$ as:

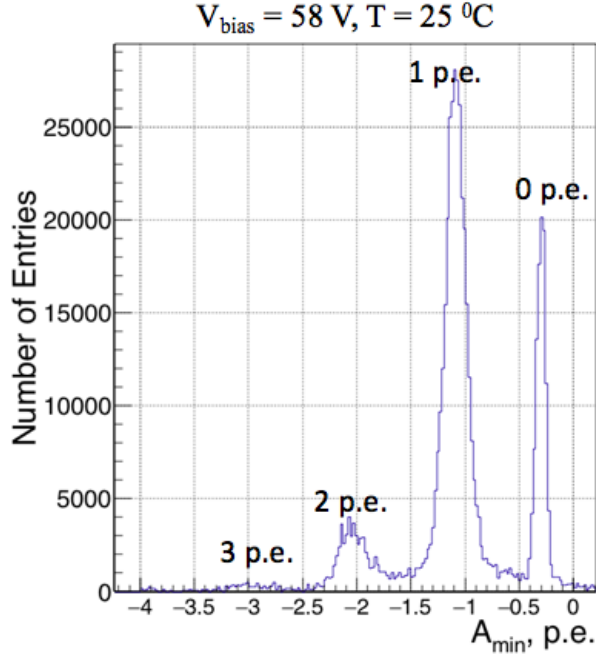


Figure 16: Local minimum of a waveform amplitude calculated within the "Dark interval".

$$P(n_{p.e.}) = \frac{\langle N_t \rangle^{n_{p.e.}}}{n_{p.e.}!} \times e^{-\langle N_t \rangle} \Rightarrow_{n_{p.e.=0}} \Rightarrow \langle N_t \rangle = -\ln(P(0)) = -\ln\left(\frac{N(0)}{N(total)}\right), \quad (31)$$

where $P(n_{p.e.})$ is the probability to detect the number of photo electrons $n_{p.e.}$, $N(0)$ and $N(total)$ are the number of events in the "0 p.e." peak and the total number, respectively.

The $\langle N_{delayed} \rangle$ can be calculated as the difference between the total number of detected SiPM pulses and $\langle N_{av}^{prim} \rangle$. Therefore, the Eq. 29 can be presented as:

$$P_{delayed} = \frac{\langle N_{total} \rangle - \langle N_{av}^{prim} \rangle}{\langle N_{total} \rangle} \quad (32)$$

The $P_{delayed}$ as a function of ΔV is presented in Fig. 17 and it is fit with the formula in Eq. 24.

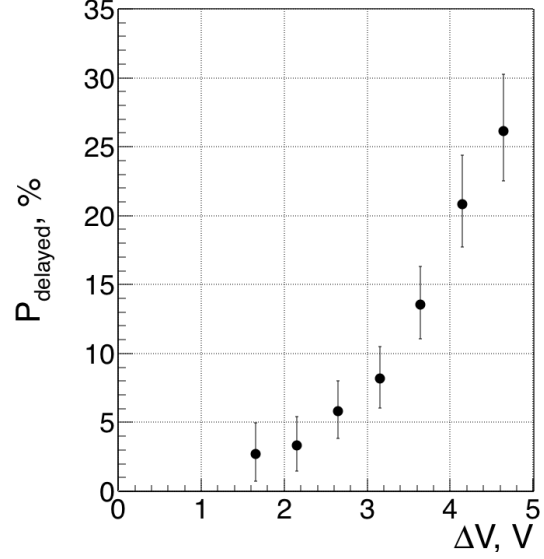


Figure 17: After-pulses and delayed cross-talk probabilities $P_{delayed}$ as a function of over-voltage.

As already mentioned in the previous section, the automatic procedure used for this data analysis can identify pulses inside a train of pulses if pulses are separated in time by ≥ 10 ns. Therefore, the after-pulse probability represented in this section is the probability to observe an after-pulse after a primary avalanche within the time interval from 10 ns up to 5 μ s.

5 Optical characterisation

The photon detection efficiency (PDE) is one of the most important parameter for the applications involving SiPM. To study the PDE as a function of ΔV as well as of the wavelength λ , our experimental setup at IdeaSquare, CERN is used (see Fig. 18a). In this Section the methods used for both absolute (at a given λ) and relative (λ dependent) PDE measurements are shown and corresponding results discussed at the end of the section.

5.1 Absolute PDE measurements with pulsed light

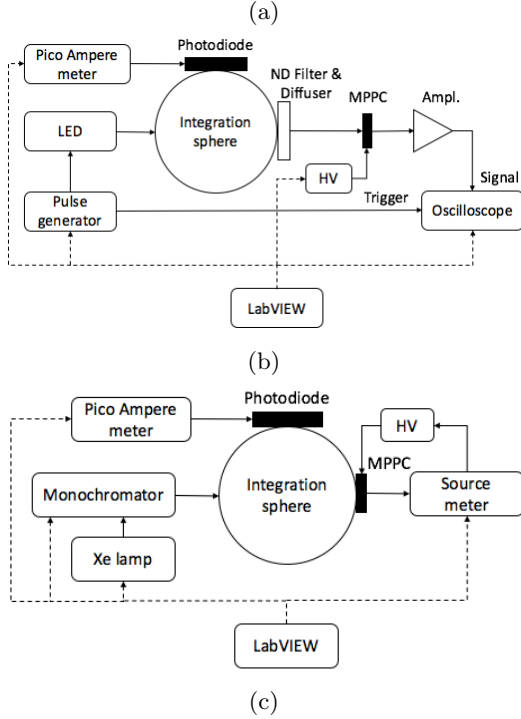
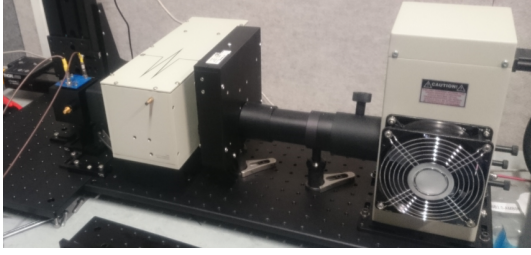


Figure 18: Developed experimental set-up for PDE measurements: 18a photo and schematic layouts for 18b absolute and 18c relative PDE measurements

The schematic layout of the experimental set-up developed for absolute PDE measurements is shown in Fig 18b. The set-up is composed by an integration sphere¹¹ to distribute uniformly and remove any directionality of the incoming light from an LED that reach the sphere output ports. The SiPM under test is placed in front of one port while on another port a calibrated photodiode¹² is used to determine the absolute amount of light which reaches the SiPM. Each LED was biased by pulse generator, with repetition rate of $f = 500$ Hz. This frequency was chosen to satisfy:

- reasonable acquisition time (around 45 minutes for

a given wavelength, for over-voltage range $1 \text{ V} \leq \Delta V \leq 8 \text{ V}$ with a step of 0.4 V);

- reasonable photocurrent level ($I_{\text{photocurrent}} \geq 100 \text{ pA}$) at least 50 times higher than dark photocurrent;
- not saturate LED.:A non linear behaviour of the LEDs was found for $f > 3 \text{ KHz}$.

The dynamic range of the SiPM, i.e. the amount of light that can be handled by it, is much lower than the one of a generic photodiode. To reduce the amount of light reaching the SiPM, a Neutral Density Filter¹³ (ND Filter) is mounted between the integration sphere output port and the SiPM. It is mounted on a motorised wheel to enable easy and fast replacement. To uniformly illuminate the SiPM full active area the 50° Square Engineered Diffuser¹⁴ is mounted after the ND Filter.

The surface is scanned with a LED of wavelength $\lambda = 405 \text{ nm}$. For this task the small photodiode¹⁵ (with 0.8 mm^2 active area) is fixed on the translation stage. The measurements of the light intensity as a function of OX and OY positions are done over a $30 \times 30 \text{ mm}^2$ area. The normalised light intensity as a function of the XY position is presented in Fig. 19 over the $12 \times 12 \text{ mm}^2$ active area of the SiPM. We measure a light intensity non-uniformity of the SiPM of less than 2%. To include this non uniformity in the PDE calculation the correction factor for the light non-uniformity α_{light} is calculated as:

$$\alpha_{\text{light}} = \frac{\int_{y_0}^{y_1} \int_{x_0}^{x_1} I_{\text{light}}(x, y) \, dx dy}{S_{\text{SiPM}}} \div \frac{\int_{-5}^5 \int_{-5}^5 I_{\text{light}}(x, y) \, dx dy}{S_{\text{PD}}}, \quad (33)$$

where $I_{\text{light}}(x, y)$ is the normalised light intensity at the x, y coordinate (See Fig. 19), S_{SiPM} and S_{PD} are the active areas of the SiPM and of the calibrated photodiode, respectively, across which the integration is done.

¹¹Thorlab, Model IS200-4

¹²Hamamatsu S1337-1010BQ, s/n 61

¹³Thorlab, Model NE530B

¹⁴Thorlab, ED1-S50-MD

¹⁵Thorlab, Model SM05PD2A

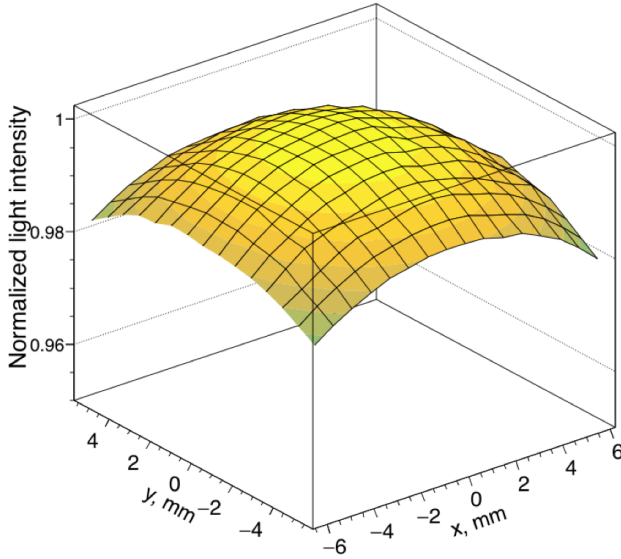


Figure 19: Normalised light intensity as a function of XY position.

The power ratio $R = P_{PD}/P_{SiPM}$ between the light intensity measured by the calibrated photodiode, P_{PD} , and the SiPM, P_{SiPM} , is measured experimentally. This is done by replacing the SiPM by another calibrated photodiode¹⁶, while the diffuser is present not to change the original light spatial position as for the SiPM. The measurements done with different LEDs of different wavelengths λ are presented in Table 3.

Wavelength (nm)	R
405	1.26×10^{-3}
420	1.35×10^{-3}
470	1.35×10^{-3}
505	1.37×10^{-3}
530	1.39×10^{-3}
572	1.38×10^{-3}

Table 3: Measured power ratios R for different LED wavelengths.

In order to correct for this effect in the PDE measurement, the transparency ($R_{ND}(n)$) of the ND Filter at a given λ is measured as:

$$R_{ND}(n) = \frac{I_{ND}(n(t_0))}{I_{PD}(t_0)} \div \frac{I_{ND}n(t)}{I_{PD}(t)}, \quad (34)$$

where n is the ND Filter number (the $n = 1$ corresponds to the situation without any filter), $I_{ND}(n(t_0))$ and $I_{ND}(n(t))$ are the photocurrents measured by the photodiode positioned after the ND Filter at time t_0 and t respectively, and $I_{PD}(t_0)$ and $I_{PD}(t)$ are the pho-

tocurrents measured by the reference photodiode positioned at another output of the integration sphere at time t_0 and t , respectively. The Xenon lamp coupled with a monochromator¹⁷ is used as a light source of a given λ . The comparison between the measured values of $R_{ND}^{Measured}(n)$ and the "typical" one given by the producer $R_{ND}^{Typical}(n)$ as a function of λ are presented in Fig. 20. The relative differences:

$$R_{ND}^{Diff.}(n) = \frac{R_{ND}^{Typical}(n) - R_{ND}^{Measured}(n)}{R_{ND}^{Measured}(n)}, \quad (35)$$

between measured and "typical" transmissions is presented in Fig. 20 (bottom).

The data acquisition system is similar to the one presented in Sec. 4.1. During data taking, the photo-current of the photodiode is read out by the Keithley 6487. Data taking is triggered by a pulse generator and controlled by a LABVIEW program to automate the necessary measurement steps.

The absolute PDE is calculated from the so-called Poisson method [8] [5]. For every waveform, the local minimum A_{min} of the waveform amplitude (we are working with negative pulses) is calculated within a time window in which the light from the LED is expected to be contained (the LED gate of $\simeq 40ns$). A typical distribution of A_{min} for waveforms acquired at $V_{bias} = 59.2$ V is presented in Fig. 21. Due to reasons already described in Sec. 4.5.3, the "0 p.e" peak is selected to determine the average number of detected photons k_{LED} eliminating any influence from cross-talk (prompt and delayed) and after-pulses:

¹⁶Hamamatsu S1337-1010BQ, s/n 1

¹⁷Oriel Tunable Light Source System TLC-75X

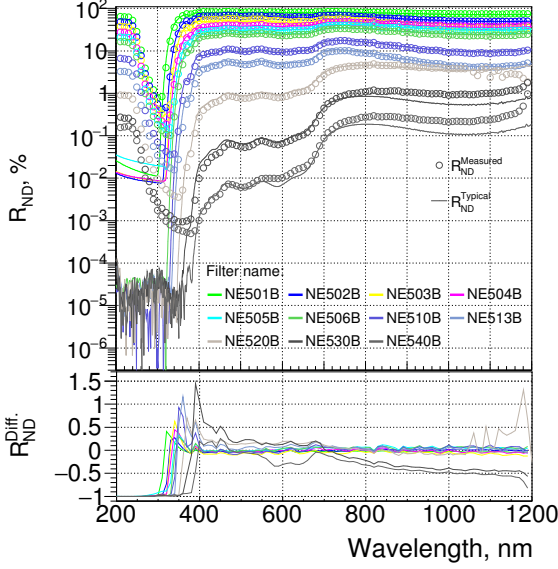


Figure 20: Measured (open dots) $R_{ND}^{Measured}(n)$ and "typical" one $R_{ND}^{Typical}(n)$ given by producer (lines) transmission of ND Filters as a function of wavelength. Also, the relative differences $R_{ND}^{Diff.}(n) = \frac{R_{ND}^{Typical}(n) - R_{ND}^{Measured}(n)}{R_{ND}^{Measured}(n)}$ are shown in bottom plot.

$$P(n_{p.e.}) = \frac{k_{LED}^{n_{p.e.}}}{n_{p.e.}!} \times e^{-k_{LED}} \Rightarrow_{n_{p.e.}=0} \Rightarrow k_{LED} = -\ln(P_{LED}(0)) = -\ln\left(\frac{N_{LED}(0)}{N_{LED}(total)}\right), \quad (36)$$

where $P(n_{p.e.})$ is the probability to detect a given number of photo electrons $n_{p.e.}$, $N_{LED}(total)$ is the total number of events. However, thermal SiPM pulses can appear within the *LED gate* used for the A_{min} calculation. Therefore the value of k_{LED} is corrected for dark SiPM pulses using an auxiliary *dark gate*. with equal length with respect to the "*LED*" *gate*, but at the beginning of a waveform, when the SiPM is operated in dark conditions):

$$k_{LED}^{corrected} = -\ln(P_{LED}(0)) + \ln(P_{dark}(0)) = -\ln\left(\frac{N_{LED}(0)}{N_{LED}(total)}\right) + \ln\left(\frac{N_{dark}(0)}{N_{dark}(total)}\right), \quad (37)$$

where $k_{LED}^{corrected}$ is the corrected average number of detected photons, $N_{dark}(0)$ and $N_{dark}(total)$ are the number of waveforms with no SiPM signal within the *dark gate* and the total number of recorded waveforms, respectively.

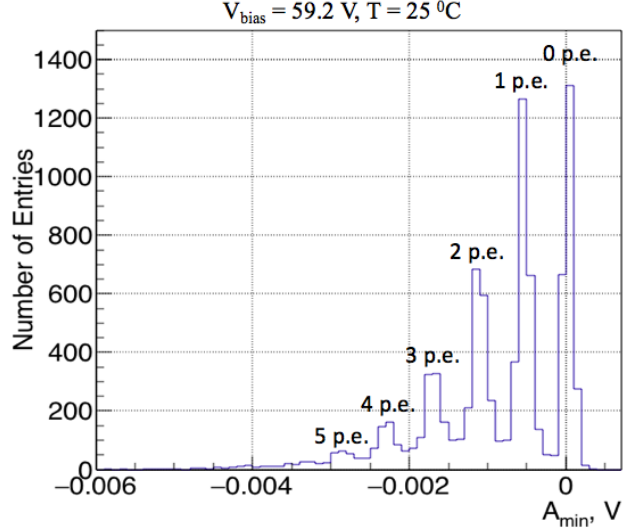


Figure 21: Local minimum of a waveform amplitude calculated within the *LED gate*, the time gate during which the pulses from the LED are expected.

Finally, the *PDE* can be calculated as:

$$PDE = \frac{k_{LED}^{corrected}}{N_{photons}}, \quad (38)$$

where $N_{photons}$ is the average number of photons hitting the SiPM. The $N_{photons}$ can be calculated from converting the photocurrent from the calibrated photodiode as:

$$N_{photons} = \frac{I_{PD} \times R \times R_{ND} \times \alpha_{light}}{f \times QE(\lambda) \times e}, \quad (39)$$

where I_{PD} is the photocurrent measured by the calibrated photodiode, $QE(\lambda)$ is the photodiode quantum efficiency, f is the pulse repetition frequency (typically $f = 500 \text{ Hz}$) and e is the electron charge. The PDE as a function of ΔV for six different wavelengths: 405 nm, 420 nm, 470 nm, 505 nm, 530 nm and 572 nm are presented in Fig.22. There are three main errors sources for the PDE determination:

- The precision on the $N_{photons}$ measurement, obtained from the current generated by the photodiode, used for the photodiode calibration curve, and corrected by the power ratio $R = P_{PD}/P_{SiPM}$ (see Tab.3).
- The determination of $k_{LED}^{corrected}$ from the separation of the "0 p.e." and "1 p.e." peaks (See Fig. 21). Affected by SiPM noise (e.g. DCR , P_{XT} and $P_{a.p.}$), which are enhanced by length of "*LED*" *gate*.
- The precision of calibrated quantum efficiency curve for photodiode.

Therefore, for precise absolute *PDE* measurements perfectly calibrated photodiodes, fast LEDs or lasers are strongly preferable.

The PDE of SiPM device is the product of three parameters: the quantum efficiency QE , the geometrical fill factor ϵ and the triggering probability P_{Geiger} :

$$PDE = QE \times \epsilon \times P_{Geiger} \quad (40)$$

Only, P_{Geiger} shows variation with ΔV . Therefore, following McIntyre [14] the PDE vs ΔV at a given λ can be parametrised as:

$$\begin{aligned} PDE &= QE \times \epsilon \times P_{Geiger} = \\ &= PDE_{max} \times [1 - \exp(-PDE_{slope} \times \Delta V)] \end{aligned} \quad (41)$$

where $PDE_{max} = QE \times \epsilon$, PDE_{slope} is the parameter depending on the SiPM design and composition of free carriers, which describes how fast PDE changes with over-voltage ΔV and has dimensions $1/Voltage$. Such a parameterisation provides a good description of our experimental data as shown in Fig. 22.

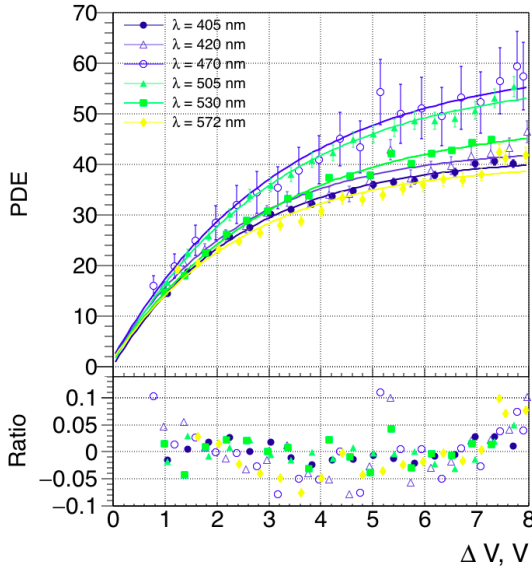


Figure 22: PDE vs. ΔV of the Hamamatsu S10943-2832(X) SiPM. The results are presented for six different wavelengths: 405 nm, 420 nm, 470 nm, 505 nm, 530 nm and 572 nm. Also, the $Ratio = (PDE_{data} - PDE_{fit}) \div PDE_{data}$ is shown.

5.2 Relative PDE measurement with continuous light

Since the absolute PDE measurements method requires a pulsed light source, the PDE is calculated only for six fixed wavelengths. Therefore, to measure the PDE in a wide wavelength range, from 280 nm up to 1150 nm, the second method, the so called "Relative PDE ", is used. The schematic layout of the experimental set-up

developed for the relative PDE measurement is shown in Fig 18c. The 75 W Xe lamp coupled with the monochromator is used. The reverse current-voltage IV characteristics of the SiPM device illuminated by various light wavelengths λ are performed using a Keithley 2400. The Keithley 6487 is used to read photocurrent from calibrated photodiode.

The collection of reverse IV curves of the Hamamatsu S10943-2832(X) SiPM illuminated by continuous light of various wavelengths from 280 nm up to 1150 nm is presented in Fig. 23. The difference between SiPM current with light and in dark condition $I_{SiPM}^{light} - I_{SiPM}^{dark}$ at a given ΔV can be expressed as:

$$\begin{aligned} I_{SiPM}^{light} - I_{SiPM}^{dark} &= \\ &= PDE(\Delta V, \lambda) \times N_\gamma \times e \times G_{SiPM}(\Delta V) \end{aligned} \quad (42)$$

where $PDE(\Delta V, \lambda)$ - is the SiPM PDE at a given ΔV and λ , N_γ - is the average number of photons sent to the SiPM device per given time interval, $G_{SiPM}(\Delta V)$ is the effective SiPM gain, namely the SiPM gain enhanced by cross-talk (prompt and delayed) and after-pulses effects (for more details see Sec. 4.1). The N_γ is proportional to the photocurrent from the calibrated photodiode $I_{PD}(\lambda)$. Therefore, the relative PDE can be presented from Eq. 42 as:

$$\begin{aligned} PDE(\Delta V, \lambda) &= \frac{I_{SiPM}^{light} - I_{SiPM}^{dark}}{e \times N_{p.e.} \times G_{SiPM}(\Delta V)} \propto \\ &\propto \frac{I_{SiPM}^{light} - I_{SiPM}^{dark}}{I_{PD}(\lambda)} \end{aligned} \quad (43)$$

The relative PDE as a function of λ at $\Delta V = 2.8$ V is presented in Fig. 24. Also, the relative PDE can be calculated from the "IV Model" (For more details see Sec. 3.2).

To calculate the relative PDE from the "IV Model", the reverse IV curves are normalised to the light intensity from the calibrated photodiode. We know that for a given SiPM device at a given temperature the $C_{\mu cell}$ and $\frac{dN_{car}}{dt}$ do not depend on light intensity, but they are related to the SiPM internal structure. Therefore, the simultaneous fit is done by Eq. 17, assuming that $C_{\mu cell}$ and $\frac{dN_{car}}{dt}$ are the same for all curves. To simplify the fit procedure, the simultaneous fit is done only for the eight curves corresponding to 300, 350, 400, 470, 550, 600, 700 and 800 nm wavelengths. However, except for computing time, there is no further limitation to use a higher number of reverse IV curves for the fitting procedure. The relative PDE calculated from the "IV Model" is in a good agreement with the results calculated from Eq. 43 as shown in Fig. 24. The main advantage to use the "IV Model" for relative PDE calculation instead of the calculation in Eq. 43 is that the "IV Model" also provides information about the breakdown voltage. In case of Eq. 43 the V_{BD} should be calculated independently

(from AC or DC measurements), to be able to present the PDE as a function of over-voltage.

To have an absolute PDE vs λ the relative PDE is normalised to the absolute values obtained from Eq.41 at $\Delta V = 2.8V$ and presented in Fig. 25. Due to the complicate behaviour of the PDE as a function of λ , we use the convolution of three polynomial functions to fit experimental data from 260 up to 1000 nm :

$$\begin{aligned}
 PDE(\lambda, \Delta V = Cons.) &= (a_1 + b_1 \cdot \lambda + c_1 \cdot \lambda^2) \cdot \\
 &\cdot \mathcal{H}_1(\lambda) \begin{cases} 1 & 260 \text{ nm} < \lambda < 370 \text{ nm} \\ 0 & \lambda < 260 \text{ nm or } \lambda > 370 \text{ nm} \end{cases} + \\
 &\quad + (a_2 + b_2 \cdot \lambda + c_2 \cdot \lambda^2) \cdot \\
 &\cdot \mathcal{H}_2(\lambda) \begin{cases} 1 & 370 \text{ nm} < \lambda < 530 \text{ nm} \\ 0 & \lambda < 370 \text{ nm or } \lambda > 530 \text{ nm} \end{cases} + \\
 &\quad + (a_3 + b_3 \cdot \lambda + c_3 \cdot \lambda^2 + d_3 \cdot \lambda^3) \cdot \\
 &\cdot \mathcal{H}_3(\lambda) \begin{cases} 1 & 530 \text{ nm} < \lambda < 1000 \text{ nm} \\ 0 & \lambda < 530 \text{ nm or } \lambda > 1000 \text{ nm} \end{cases} \quad (44)
 \end{aligned}$$

where a_i, b_i, c_i , with $i = 1, 2, 3$, and d_3 - are 10 free parameters and \mathcal{H}_i is the Heaviside step functions. Good agreement between experimental data and this approximation can be found in Fig. 25.

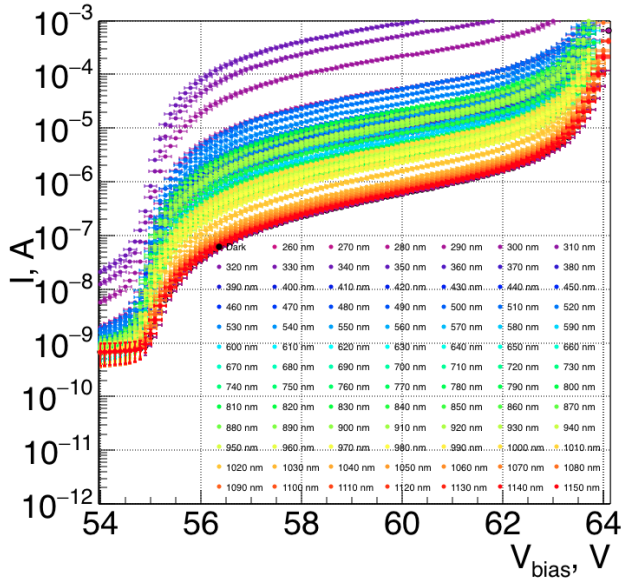


Figure 23: The reverse IV measurements of the Hamamatsu S10943-2832(X) SiPM illuminated by continuous light for various wavelengths from 260 nm up to 1150 nm.

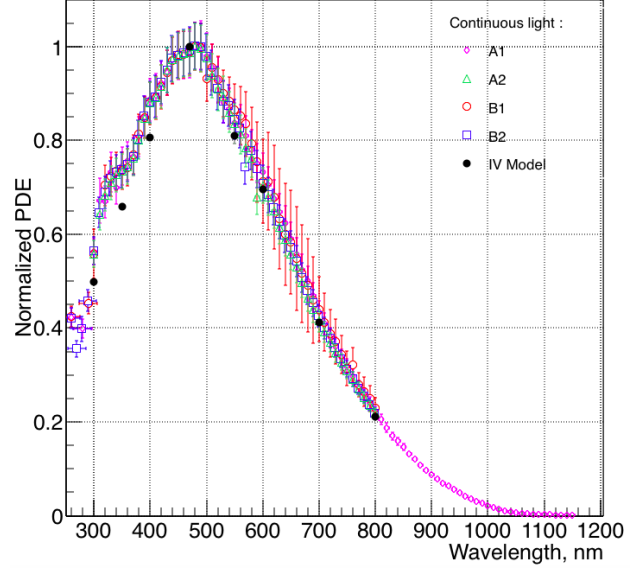


Figure 24: The relative PDE vs λ for the Hamamatsu S10943-2832(X) SiPM. The results are presented for all four channels: A1, B1, A2 and B2. Also the PDE calculated from the “IV Model” for the A1 channel is presented using black points.

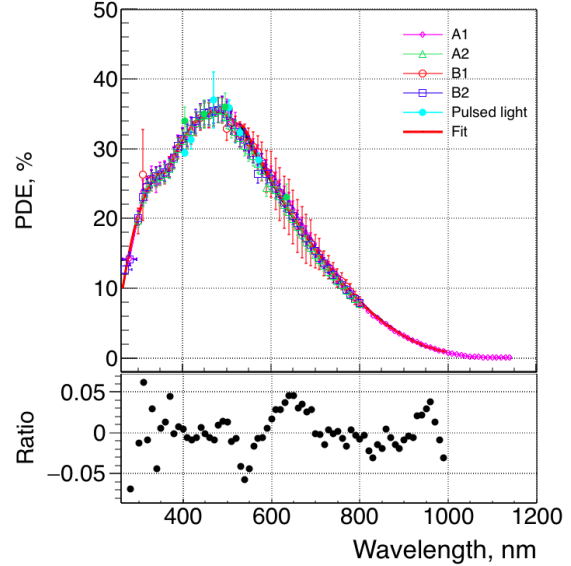


Figure 25: The PDE vs wavelength for the Hamamatsu S10943-2832(X) SiPM from 260 nm up to 1000 nm at $\Delta V = 2.8V$. Each channel is presented by a different colour and the PDE from pulsed light is presented by cyan dots. Also the fit is shown by the red line and the $Ratio = (PDE_{data} - PDE_{fit}) \div PDE_{data}$ is shown in the bottom plot.

The absolute PDE can be calculated at any over-

voltage from Eq.41. At the same time, the shape of the relative PDE can be calculated at any over-voltage below the “second breakdown” from IV curves. Both the absolute and relative $PDEs$ as a function of ΔV and λ are shown in Fig. 26. The PDE as a function of ΔV and λ can be used to predict the change of PDE with variations of experimental conditions, effect with affect ΔV , like temperature or night sky background for cameras of gamma-ray telescopes such as the one where we employed the examined sensor. The analytical expression of $PDE = f(\lambda, \Delta V)$ can be given as:

$$\begin{aligned} PDE(\Delta V, \lambda) &= \\ &= PDE_{Max}(\lambda) \times P_{Geiger}(PDE_{slope}(\lambda, \Delta V)) \quad (45) \end{aligned}$$

where $PDE_{Max}(\lambda)$ is the free parameter defining the PDE saturation and given by Eq. 44, $P_{Geiger}(PDE_{slope}(\lambda, \Delta V))$ is the Geiger probability (See Eq. 14). The PDE_{slope} as a function of λ is well represented by a polynomial of 3^d order. As a matter of fact, the agreement with this representation is on average of less than 3 % (see Fig. 27). The biggest disagreements related to low over-voltages ($\Delta V \leq 1.5 V$), especially for:

- $\lambda \leq 300 nm$, in this range the Xe lamp was operated with 1.24 mm slit width (to deliver reasonable light level). It led in 16.1 nm wavelength resolution, what results to poor precision of calculated PDE (See Fig. 25) and respectively to poor agreement with fit function
- $\lambda \geq 800 nm$, in this range photocurrent generated by SiPM is very close to its dark current (please see Fig. 23). Therefore, the signal to noise ratio is low in this λ range.

From the fit the PDE_{slope} vs. λ is calculated and presented in the Fig. 28. This parameter can be used to calculate the P_{Geiger} at any λ or ΔV as it will be presented in the next section (5.3).

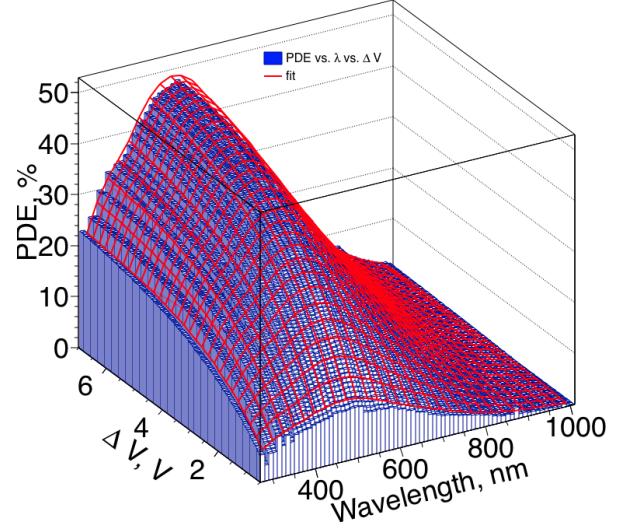


Figure 26: The PDE vs. λ and ΔV for S10943-2832(X).

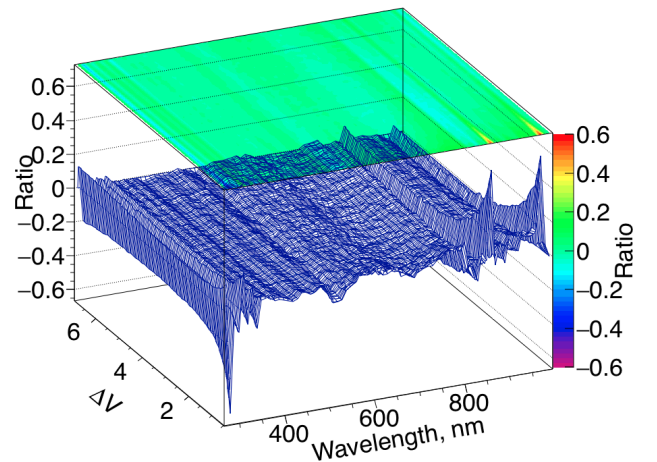


Figure 27: The difference between the measured PDE and the fit function divided by the measured PDE.

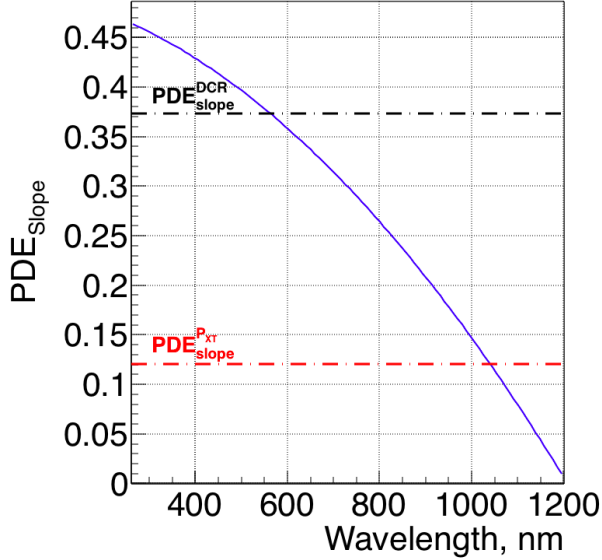


Figure 28: The PDE_{slope} as a function of λ . Also, the PDE_{slope} obtained from the DCR and the P_{XT} measurements are presented.

5.3 Geiger probability, P_{Geiger}

Geiger probability P_{Geiger} , also known as triggering probability, represents the probability that a carrier reaching the high field region will trigger an avalanche. The P_{Geiger} is calculated from a part of PDE fit (See Eq. 41) and PDE_{slope} as:

$$P_{Geiger}(\lambda, \Delta V) = 1 - \exp(PDE_{slope}(\lambda) \times \Delta V) \quad (46)$$

The P_{Geiger} as a function of ΔV for different wavelengths λ is presented in Fig. 29. We can observe that P_{Geiger} increases with increasing ΔV much faster for short λ (blue light) than for long λ (red light). This behaviour is related to the properties of light absorption in silicon and to the SiPM micro-cell structure: $p^+/n/n - epi/n - sub$ and electrons α_e and holes α_h ionisation rates. Following Oldham [22], the P_{Geiger} is a combination of electrons P_e and holes P_h triggering probabilities:

$$P_{Geiger} = P_e + P_h - P_e \times P_h \quad (47)$$

The $p^+/n/n - epi/n - sub$ structure SiPM has two boundary conditions:

$$P_e(d) = 0 \quad (48)$$

$$P_h(0) = 0 \quad (49)$$

where d is the depletion thickness of micro-cell.

From these boundary conditions we can assume that P_{Geiger} at short λ (blue light) represented only by P_e , while P_{Geiger} at long λ (red light) represented only by P_h .

Following Oldham [22] and McIntyre [14] P_e increases with increasing ΔV much faster with respect to P_h (i.e. $\alpha_e \gg \alpha_h$) as we can observe in Fig. 29.

The average probability that thermal pulses (see Sec. 4.5.1) or pulses created by optical cross-talk (see Sec. 4.5.2) trigger an avalanche are presented as P_{Geiger}^{DCR} and $P_{Geiger}^{P_{XT}}$ in Fig.29. It is found that P_{Geiger}^{DCR} is equal to P_{Geiger} at $\lambda = 565$ nm, while $P_{Geiger}^{P_{XT}}$ is equal to P_{Geiger} at $\lambda = 1041$ nm from PDE_{slope} . Knowing the absorption depth in Si at these wavelengths which is $1.7 \mu m$ for 565 nm and $440 \mu m$ for 1041 nm we may conclude that:

- the main contribution of DCR is coming from carriers thermally generated in the $n - epi$ layer. Since the measured device has a $p^+/n/n - epi/n - sub$ micro-cell structure of $1.9 \mu m$ depletion thickness (see Sec. 4.4), the $1.7 \mu m$ depth should correspond to the $n - epi$ layer;
- the main contribution of P_{XT} is coming from photons (emitted due to hot carrier luminescence phenomena) penetrated down to the end of the $n - sub$ layer, where they are reflected back into the active area and trigger secondary avalanches ($440 \mu m$ correspond to the typical SiPM thickness);

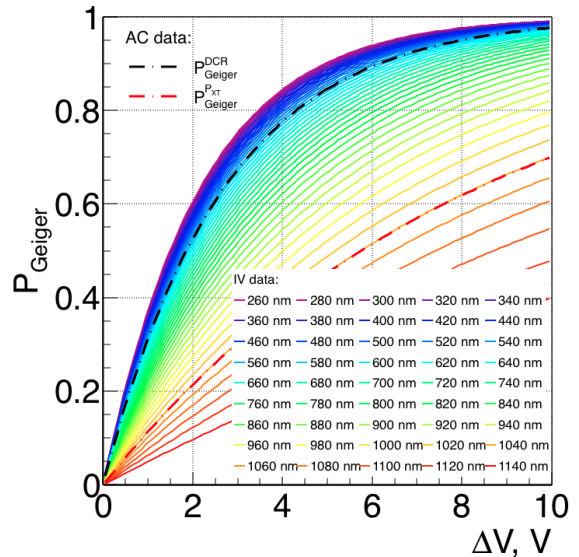


Figure 29: P_{Geiger} as a function ΔV for various λ . Also the average P_{Geiger} for DCR and for P_{XT} are shown.

6 Conclusions

In this paper we report about the full characterisation measurements of the large area hexagonal SiPM S10943-2832(X). We measured SiPM parameters like: breakdown voltage V_{BD} , dark count rate DCR , optical

cross-talk P_{XT} and after-pulse probability P_{ap} , triggering probability P_{Geiger} , photon detection efficiency PDE as a function of overvoltage ΔV and wavelength λ . All, these characteristics are detailed in Tab. 4. Additionally, we compared several methods commonly used for V_{BD} calculation from reverse current voltage IV measurements. The functions to fit PDE , DCR and P_{XT} are proposed. Moreover, from these fits, the regions that mostly contribute carriers and photons, respectively, to DCR and P_{XT} , are found.

Breakdown voltage V_{BD}^{AC}	$54.70 \pm 0.02 \pm 0.03$ V
DCR/mm^2 @ 0.5p.e. (@ V_{op})	26.50 ± 0.15 KHz
DCR/mm^2 @ 1.5p.e. (@ V_{op})	1.735 ± 0.04 KHz
P_{XT} (@ V_{op})	6.5 %
P_{ap} (@ V_{op} within 5 μs)	8.4 ± 2.1 %
PDE (@ V_{op} & $\lambda = 472$ nm)	35.5 ± 3.5 %
Peak sensitivity wavelength	480 nm
Quenching resistor R_q	$249.4 \pm 0.8 \pm 1.3$ k Ω

Table 4: S10943-2832(X) SiPM main measured characteristics at $T = 25$ °C. $V_{op} = V_{BD} + 2.8$ V.

Acknowledgements

We acknowledge the support of the SNF funding agency and of the SENSE European Community FETOPEN-CSA-FETEXCHANGE-2015 project (<http://sense-pro.org>). This paper has gone through internal review by the CTA Consortium.

References

[1] A. Nagai, N. Dinu and A. Para (2015). Breakdown voltage and triggering probability of sipm from iv curves. *NSS/MIC*, pages 1–4.

[2] Aguilar, J., Bilnik, W., Borkowski, J., Cadoux, F., Christov, A., della Volpe, D., Favre, Y., Heller, M., Kasperek, J., Lyard, E., Marszaek, A., Moderski, R., Montaruli, T., Porcelli, A., Prandini, E., Rajda, P., Rameez, M., Schioppa, E., Pujadas, I. T., Zitara, K., Bocki, J., Bogacz, L., Bulik, T., Curyo, M., Dyrda, M., Frankowski, A., Grudniki, ., Grudziska, M., Idkowski, B., Jamrozy, M., Janiak, M., Lalik, K., Mach, E., Mandat, D., Michaowski, J., Neronov, A., Niemiec, J., Ostrowski, M., Pasko, P., Pech, M., Schovanek, P., Seweryn, K., Skowron, K., Sliusar, V., Sowiski, M., Stawarz, ., Stodulska, M., Stodulski, M., Toscano, S., Walter, R., Wicek, M., Zagdaski, A., and ychowski, P. (2016). The front-end electronics and slow control of large area sipm for the sst-1m camera developed for the

cta experiment. *Nuclear Instruments and Methods in Physics Research Section A: Accelerators, Spectrometers, Detectors and Associated Equipment*, 830:219 – 232.

- [3] A.L. Lacaita et al. (1993). *On the bremsstrahlung origin of hot-carrier-induced photons in silicon devices*. *IEEE Trans. on Elect. Devices*, 40:577.
- [4] Bonanno, G., Marano, D., Belluso, M., Billotta, S., Grillo, A., Garozzo, S., Romeo, G., and Timpanaro, M. C. (2014). Characterization measurements methodology and instrumental set-up optimization for new sipm detectorspart i: Electrical tests. *IEEE Sensors Journal*, 14(10):3557–3566.
- [5] Chaumat, V., Bazin, C., Dinu, N., Puill, V., and Vagnucci, J.-F. (2012). Absolute photo detection efficiency measurement of silicon photomultipliers.
- [6] E. Garutti, M. Ramilli, C. Xu and L. Hellweg (2014). *Characterization and X-Ray damage of Silicon Photomultipliers*. *PoS(TIPP2014)070*.
- [7] E. H. Hall (1879). *On a New Action of the Magnet on Electric Currents*. *American J. of Math.*, 2(3):287.
- [8] Eckert, P., Schultz-Coulon, H.-C., Shen, W., Stamen, R., and Tadday, A. (2010). Characterisation studies of silicon photomultipliers. *Nuclear Instruments and Methods in Physics Research Section A: Accelerators, Spectrometers, Detectors and Associated Equipment*, 620(2):217 – 226.
- [9] J. Bude, N. Sano, A. Yoshii (1992). Hot-carrier luminescence in Si. *Physical Review B*, 45(11):5848–5856.
- [10] J. Frenkel (1938). *On Pre-Breakdown Phenomena in Insulators and Electronic Semi-Conductors*. *Phys. Rev.*, 54:647.
- [11] J.A. Aguilar, A. Basili, V. Boccone, F. Cadoux, A. Christov, D. della Volpe, T. Montaruli, L. Platos and M. Rameez (2015). *Design, optimization and characterization of the light concentrators of the single-mirror small size telescopes of the Cherenkov Telescope Array*. *Astrop. Phys.*, 60:32.
- [12] M. Heller et al. (2017). An innovative silicon photomultiplier digitizing camera for gamma-ray astronomy. *The European Physical Journal C*, 77(1):47.
- [13] M. Simonetta et al. (2016). Test and characterisation of SiPMs for the MEGII high resolution Timing Counter. *Nuclear Instruments and Methods in Physics Research A*, 824:145.
- [14] McIntyre, R. J. (1961). *theory of microplasma instability in silicon*. *J. Appl. Phys.*, 32:983.

- [15] N. Dinu, A. Nagai and A. Para (2017). Breakdown voltage and triggering probability of SiPM from $\{IV\}$ curves at different temperatures. NIMA, 845:64. Proc. of the Vienna Conf. on Instr. 2016.
- [16] N. Ferenc, G. Hegyesi, K. Kalinka and J. Molnár (2017). A model based $\{DC\}$ analysis of sipm breakdown voltages. Nuclear Instruments and Methods in Physics Research Section A: Accelerators, Spectrometers, Detectors and Associated Equipment, 849:55.
- [17] N. Serra et al. (2011). Experimental and TCAD Study of Breakdown Voltage Temperature Behavior in n^+/p SiPMs. IEEE Trans. on Nucl. Sci., 58(3):1233.
- [18] Nagai, A. (2013). Silicon photomultiplier for medical imaging, analysis of sipm characteristics. pages 43–46.
- [19] Para, A. (2015). Afterpulsing in Silicon Photomultipliers: Impact on the Photodetectors Characterization.
- [20] Shockley, W. (1949). The theory of p-n junctions in semiconductors and p-n junction transistors. pages 435–489.
- [21] Sun, Y. and Maricic, J. (2016). Sipms characterization and selection for the dune far detector photon detection system. Journal of Instrumentation, 11(01):C01078.
- [22] W. G. Oldham, R.R. Samuelson, P. Antognetti (1972). Triggering Phenomenain Avalanche Diodes. IEEE Trans. on Elect. Devices, 19:1056–1060.
- [23] W. Shockley and W.T. Read (1952). Statistics of the Recombinations of Holes and Electrons. Phys. Rev., 87:835.
- [24] Z. Guoqing, H. Dejun, Z. Changjun and Z. Xuejun (2012). Turn-on and turn-off voltages of an avalanche pn junction. J. of Semiconductors, 33(9):094003.